# Computational Insight Into the Hydroamination of an Activated Olefin, As Catalyzed by a 1,2,4-Triazole-Derived Nickel(II) N-Heterocyclic Carbene Complex

Ravi Kumar,[†] Madanakrishna Katari,[†] Ajay Choudhary, Gopalan Rajaraman,*[ID] and Prasenjit Ghosh*[ID]

Department of Chemistry, Indian Institute of Technology Bombay, Powai, Mumbai−400 076, India

S *Supporting Information*

ABSTRACT: A density functional theory (DFT) investigation performed at the B3LYP/TZVP//B3LYP/6-31G(d)-LANL2DZ level of theory on the hydroamination of dimethylamine (Me_2NH) on an activated olefin (namely, acrylonitrile (CH_2=CHCN)), as catalyzed by a 1,2,4-triazol based nickel(II) N-heterocyclic carbene complex (namely, [1,4-dimethyl-1,2,4-triazole-5-ylidene]$_2$ nickel dichloride) revealed that the olefin coordination pathway is favorable over the amine coordination pathway, although the initial olefin coordination step is higher in energy than the initial amine coordination step. Significantly enough, the reaction involved a crucial 1,3-proton transfer step between the resonance intermediates, i.e., the C-bound $[(NHC)_2Ni(CH(CN)CH_2NHMe_2)]^+$ (**D**) species or N-bound $[(NHC)_2Ni(NCCHCH_2NHMe_2)]^+$ (**E**) species and the intermediate $[(NHC)_2Ni(NCCH_2CH_2NMe_2)]^+$ (**F**), depicting the cleavage of a N−H bond and the formation of a C−H bond facilitated by a water-assisted/amine-assisted proton shuttle. Overall, among the various pathways explored, the lowest energy pathway involved alkene coordination, followed by an amine-assisted 1,3-proton transfer step.
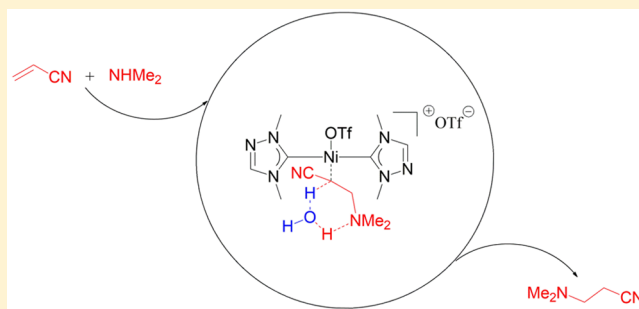
INTRODUCTION

The hydroamination of alkenes poses a formidable challenge in contemporary homogeneous catalysis, because of its thermoneutral nature. However, the significance of a 100% atom economy reaction—which has widespread applications in the fine-chemical, pharmaceutical, and agricultural industries—makes the hydroamination reaction an attractive cause to pursue.[1] A conceptual obstacle to the reaction stems from the electron richness of the reacting substrates (namely, the olefin and the amine), which makes them averse to mutually reacting on their own, in the absence of a catalyst. In this context, the Lewis-acidic transition-metal-catalyzed alkene hydroamination reactions gain relevance.[2] It is worth mentioning that the alkene hydroamination reaction is more challenging than the related alkyne hydroamination reaction, because the former is thermoneutral while the latter is favorable by −17 kcal/mol.[3] Apart from the thermoneutrality, the other issue with the alkene hydroamination reaction is that of the product selectivity. It arises from the regioselectivity in the amine addition that yields the Markovnikov and anti-Markovnikov products, along with the competing amine oxidation products formed under the reactions conditions.[4] The challenge of overcoming the difficulty associated with the reaction thermoneutrality and the promise of a wider applicability of the hydroamination reaction attracted our attention, against the backdrop of a handful of studies[5] that exist.

As a part of our larger interest in exploring the utility of the transition-metal-based N-heterocyclic carbene complexes in

chemical catalysis[2e,6] and in biomedical applications,[6d,7] we became interested in designing N-heterocyclic carbene-based catalysts for the hydroamination reactions of alkenes[8] and alkynes.[9] In addition, with the intent of designing more-efficient catalysts through a better understanding of the reaction mechanism, we decided to undertake a computation study of the alkene hydroamination reaction, as performed by a nickel precatalyst of a simplified 1,2,4-tirazole-derived N-heterocyclic carbene ligand, based on our earlier study.[8] The further motivation for the work came from our prior computational investigation on a related alkyne hydroamination reaction[10] that highlighted a critical role played by the adventitious water molecules present in the reaction medium in bringing about a drastic reduction of the activation barrier of a pivotal 1,3-proton transfer step through a water-assisted proton shuttle mechanism; hence, we wanted to determine whether such a proton relay mechanism is operational in the analogous alkene hydroamination reaction.

In this manuscript, we report a density functional theory (DFT) study of the alkene hydroamination reaction for two representative substrates, namely, CH_2=CHCN and Me_2NH, as catalyzed by a nickel catalyst (namely, *trans*-[1,4-dimethyl-1,2,4-triazol-5-ylidene]$_2$NiCl$_2$) of a simplified 1,2,4-triazole-derived N-heterocyclic carbene ligand:
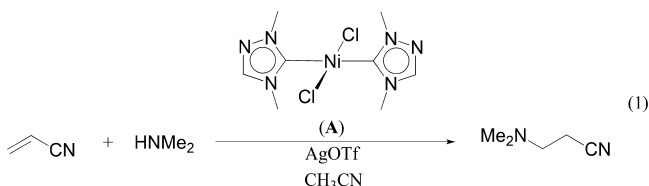
This study aims at obtaining key insights into the catalyst mode of action for the alkene hydroamination reaction.

RESULTS AND DISCUSSIONS

A computational investigation of the mechanism of the alkene hydroamination reaction with an amine as catalyzed a nickel N-heterocyclic carbene complex was undertaken using DFT study based on our prior study.[8] In particular, the catalytic cycle of an alkene hydroamination reaction was modeled for two representative substrates, namely, acrylonitrile ($CH_2=CHCN$) and dimethylamine (Me_2NH), as catalyzed by a simplified nickel catalyst, *trans*-[4-dimethyl-1,2,4-triazol-5-ylidene]$_2$NiCl$_2$ (**A**). The simplified nickel catalyst **A** contained methyl substituents instead of the isopropyl and ethyl substituents, and was so chosen for the sake of computational simplicity [see Scheme 1]. On the basis of the mass spectrometric evidence,[8] a cationic acetonitrile solvent coordinated intermediate, {[1,4-dimethyl-1,2,4-triazol-5-ylidene]$_2$Ni(NCCH$_3$)(OTf)}$^+$ (**B**), was taken to be the initiating active species of the alkene hydroamination reaction. The DFT calculations were performed on all of the intermediate species (**B**−**F**), as an isolated cationic species in the gas and the solvent phases, as opposed to the real-life ion pair scenarios that exist in solutions under experimental reaction conditions.

The characterizations of the stationary points and transition states of the proposed catalytic cycle were performed for the nickel N-heterocyclic carbene complex at B3LYP/6-31G(d)-LANL2DZ level of theory by applying suitable modifications to the structures of the precatalysts, namely, *trans*-[1-*i*-propyl-4-R-1,2,4-triazol-5-ylidene]$_2$MBr$_2$ [R = Et, CH$_2$CH = CH$_2$; M = Ni, Pd], as obtained from single-crystal X-ray diffraction studies [see Scheme 2]. The solvation effects were included using polarizable continuum model (PCM) calculations. The single-point energy calculations were performed on optimized geometries using a higher triple-ζ basis set at B3LYP/TZVP//B3LYP/6-31G(d)-LANL2DZ level of theory for obtaining good numerical estimates of the computational results. Furthermore, the charge decomposition analysis (CDA) studies were performed on all of the stationary points (**B**−**F**) of both the alkene and amine coordination pathways to investigate the metal−ligand *donor*−*acceptor* interactions [*acceptor* = [(NHC)$_2$Ni(OTf)]$^+$ in **B**−**F**, while *donor* = CH$_3$CN in **B**, CH$_2$=CHCN in **C**, NHMe$_2$ in **C'**, CNCH=CH$_2$···NHMe$_2$ in **C''**, C-bound CH(CN)CH$_2$NHMe$_2$ in **D**, N-bound CH(CN)-CH$_2$NHMe$_2$ in **E**, and NCCH$_2$CH$_2$NMe$_2$ in **F**] occurring in these species. Subsequently, the molecular orbital (MO) correlation diagrams were constructed from the individual fragment molecular orbitals (FMOs) for further understanding of these interactions. An insight into the relative extent of the forward σ-donation and the π-back-donation occurring between the *donor* and *acceptor* fragments [*acceptor* = [(NHC)$_2$Ni(OTf)]$^+$ in **B**−**F**, while *donor* = CH$_3$CN in **B**, CH$_2$=CHCN in **C**, NHMe$_2$ in **C'**, CNCH=CH$_2$···NHMe$_2$ in **C''**, C-bound CH(CN)CH$_2$NHMe$_2$ in **D**, N-bound CH(CN)CH$_2$NHMe$_2$ in **E** and NCCH$_2$CH$_2$NMe$_2$ in **F**] were obtained from *d*/*b* ratio values, in which *d* represents *donor* → *acceptor* σ-interaction, and *b* represents the complementary *acceptor* → *donor* π-interaction. Finally, free-energy (ΔG) plots of the catalytic cycle at the B3LYP/TZVP//B3LYP/6-31G(d)-LANL2DZ level of theory were constructed for the solvent phase and have been included in the discussion.

A catalytic cycle for the hydroamination reaction is envisaged to proceed through two possible pathways, namely, (i) an

Scheme 1
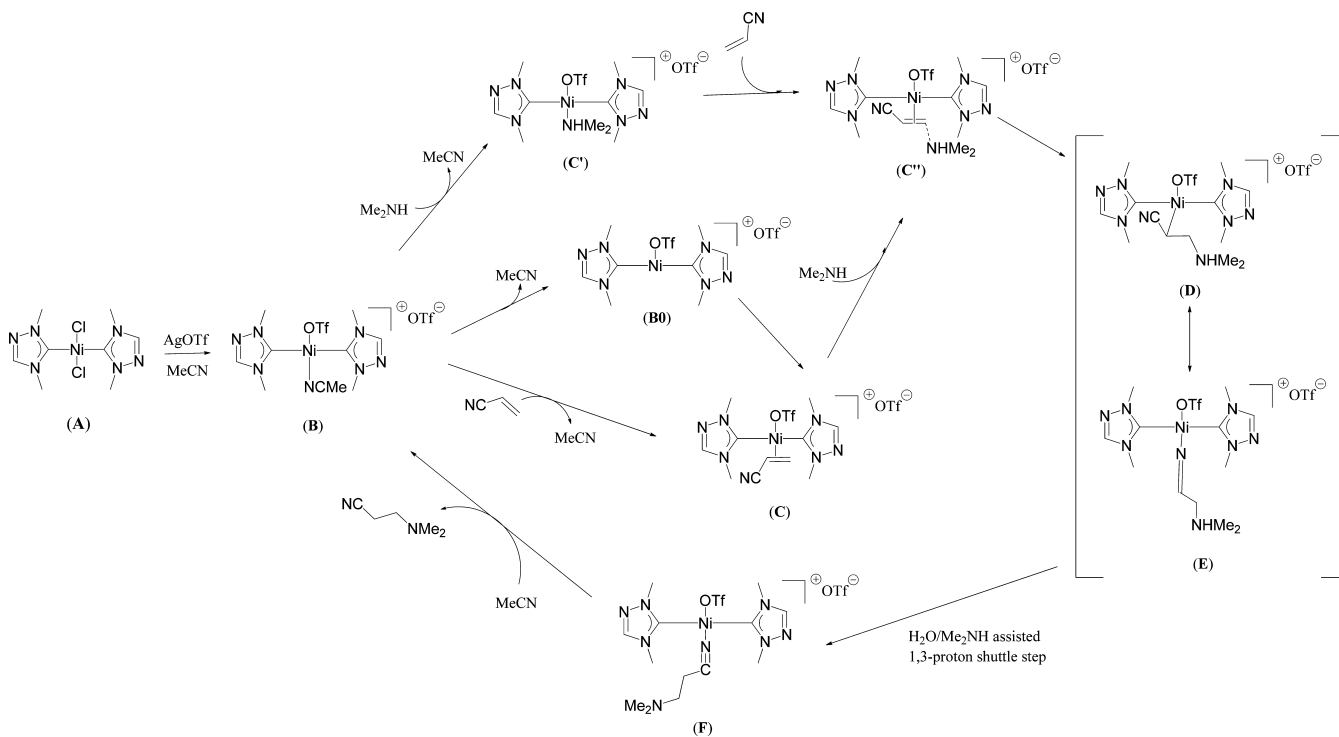
Scheme 2. Computed Catalytic Cycle for Hydroamination of CH$_2$=CHCN with NHMe$_2$ by Species A Depicting Both the Amine and Alkene Coordination Pathways Proceeding via (a) a H$_2$O-Mediated Proton-Transfer Step and (b) a NHMe$_2$-Mediated Proton-Transfer Step

(a)

(b)
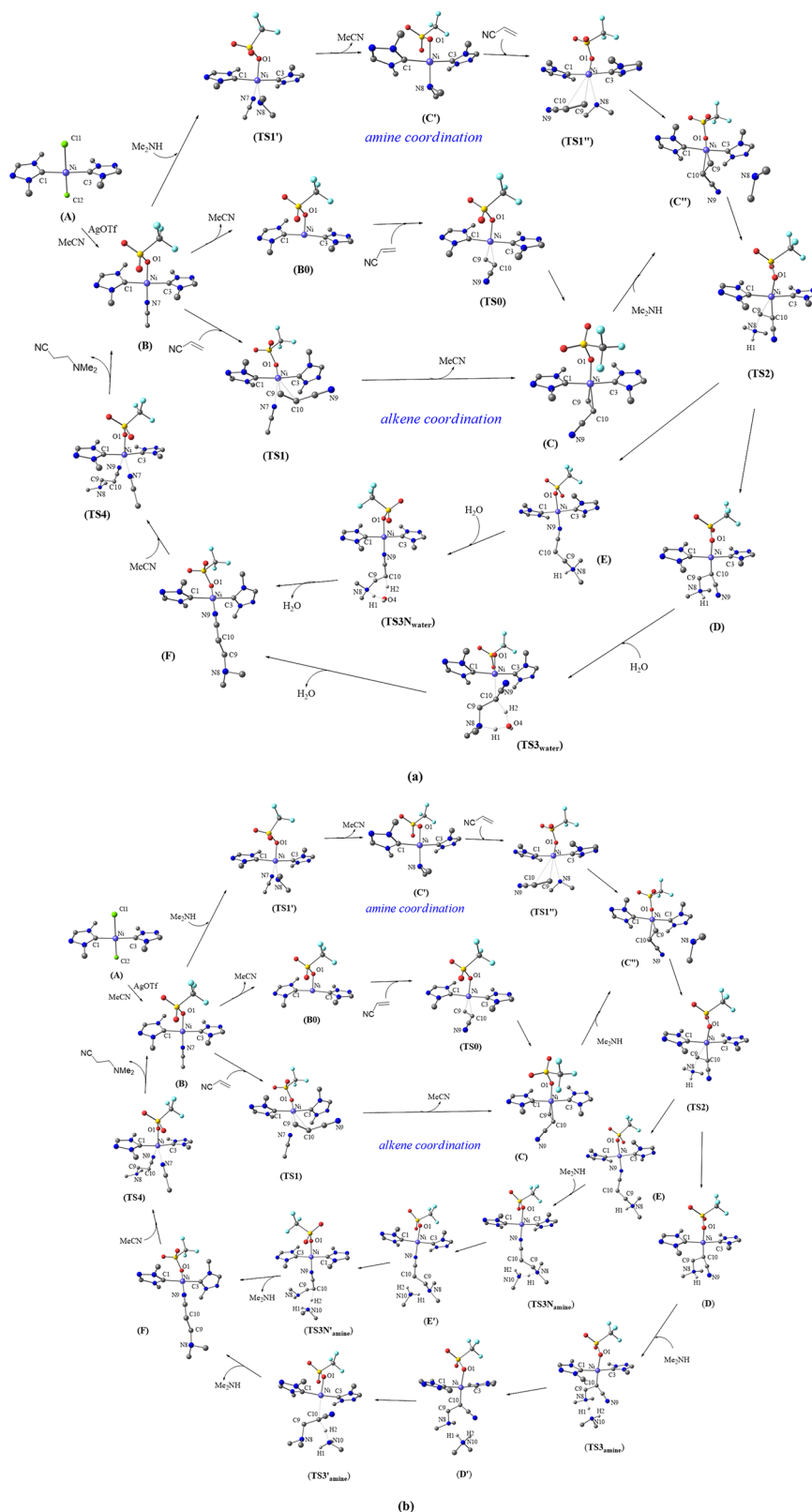
alkene coordination pathway and (ii) an amine coordination pathway. These two pathways have been examined for the nickel precatalyst, *trans*-[1,4-dimethyl-1,2,4-triazol-5-ylidene]$_2$NiCl$_2$ (**A**). The computed structure of species **A** showed the Ni

center in a square-planar geometry being bonded to two NHC ligands and two Cl ligands in a *trans* fashion [see Figure S1 in the Supporting Information]. The two Ni−C$_{carbene}$ distances are identical in species **A** [of 1.952 Å each] and are slightly longer

than the sum of the individual covalent radii of Ni and C atoms (1.86 Å).[11] The angles in species **A** at the Ni center are close to the expected value of 90°, in concurrence with the square planar geometry of the species. The natural bond orbital (NBO) analysis revealed that the two metal−carbene bonds are polar in nature, exhibiting an orbital contribution of ca. 18% from the nickel-based atomic orbitals and of ca. 82% from the carbon-based atomic orbitals.

Species **A** readily reacts with AgOTf in CH_3CN to give a precipitate of AgCl, along with an CH_3CN coordinated intermediate species $[(NHC)_2Ni(NCCH_3)(OTf)]^+$ (**B**), which is considered to be the initiating active species for the catalytic cycle. The intermediate **B** also has the expected square planar geometry [see Figure 1a]. The Ni−$C_{carbene}$ bond distances [Ni−C1 = 1.959 Å and Ni−C3 = 1.953 Å] are slightly elongated, compared to the sum of individual covalent bond radii for Ni−C [1.86 Å].[11] The polarity of the Ni−$C_{carbene}$ bonds in intermediate **B** was similar to that observed for species **A**. The Ni−$C_{carbene}$ bonds in intermediate **B** were composed of an ~21% contribution from the nickel-based atomic orbitals and an ~79% contribution from the $C_{carbene}$-based atomic orbitals. The CDA analysis gave a d/b value of 6.1, which

indicated the presence of a strong σ-bonding interaction between CH_3CN (*donor*) fragment and the $[(NHC)_2Ni(OTf)]^+$ (*acceptor*) fragment in the $[(NHC)_2Ni(NCCH_3)(OTf)]^+$ (**B**).

The Ni−$NCCH_3$ bond dissociation energy (D_e), computed at B3LYP/TZVP//B3LYP/6-31G(d)-LANL2DZ level of theory, was estimated to be 44.9 kcal/mol in the acetonitrile solvent, and is in agreement with a significantly strong binding of the CH_3CN moiety to the Ni center in intermediate **B**. The molecular orbital (MO) correlation diagram constructed for the $[(NHC)_2Ni(OTf)]^+$ (*acceptor*)−CH_3CN (*donor*) interaction in the intermediate **B** revealed that the Ni−N7 bond was comprised of σ-type donation from the nitrogen lone pair of the CH_3CN moiety to the d-type FMOs of $[(NHC)_2Ni(OTf)]^+$ [see Figure 2]. The intermediate **B** can further proceed via two different routes, i.e., the alkene coordination pathway and amine coordination pathway in the alkene hydroamination reaction.

Alkene Coordination Pathway. This pathway involves the CH_3CN coordinated intermediate **B** reacting with the olefin substrate $CH_2{=}CHCN$, with the elimination of a free CH_3CN molecule to yield an alkene-coordinated intermediate $[(NHC)_2Ni(CH_2{=}CHCN)(OTf)]^+$ (**C**). Here, we have
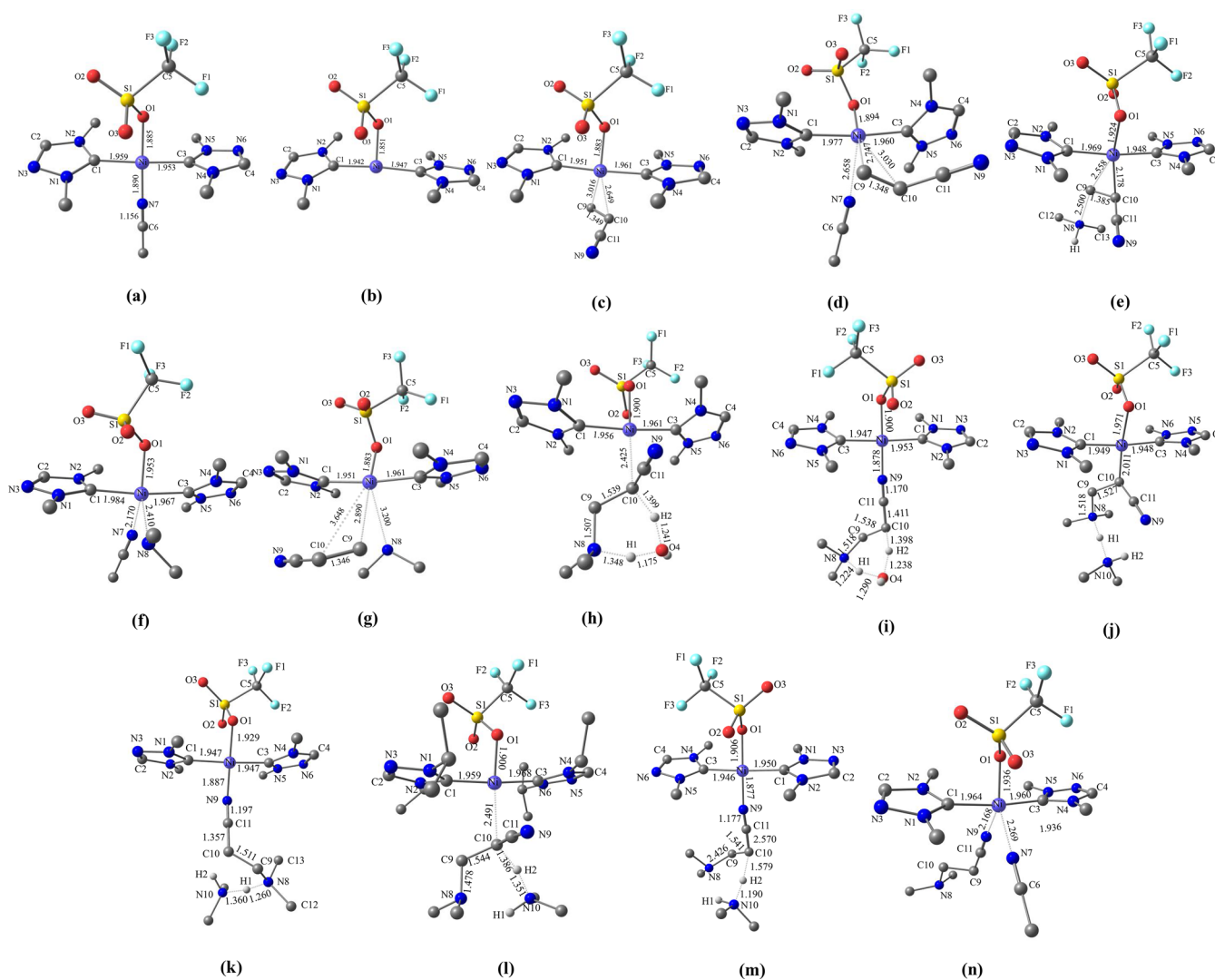

Figure 1. Computed structures of (a) **B**, (b) **B0**, (c) **TS0**, (d) **TS1**, (e) **TS2**, (f) **TS1'**, (g) **TS1''**, (h) **TS3$_{water}$**, (i) **TS3N$_{water}$**, (j) **TS3$_{amine}$**, (k) **TS3N$_{amine}$**, (l) **TS3'$_{amine}$**, (m) **TS3N'$_{amine}$**, and (n) **TS4**. Selected bond lengths are given in Å. (H atoms are omitted for the sake of clarity).
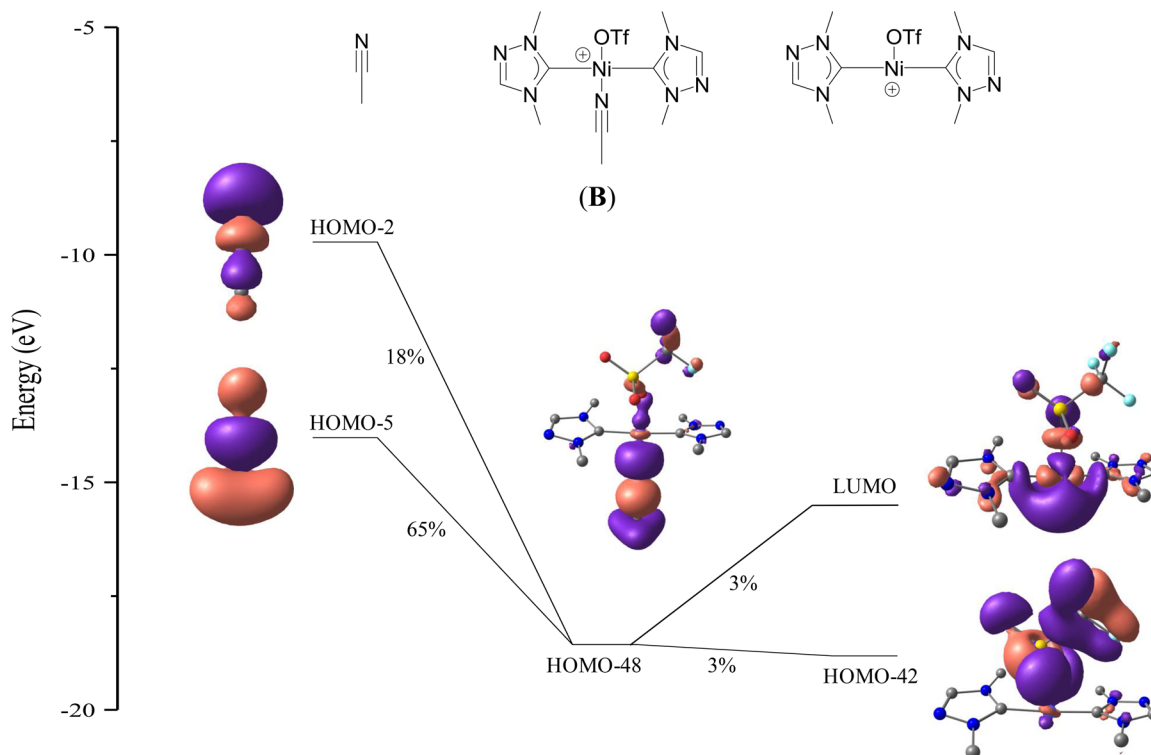
Figure 2. A simplified orbital interaction diagram showing the major contributions of the $[(NHC)_2(OTf)Ni-NCMe]^+$ bond in **B**.

explored both associative and dissociative pathways for intermediate **B** to generate intermediate **C**.

In the dissociative pathway, the Ni−NCMe bond would cleave to form a three-coordinate intermediate $[(NHC)_2Ni(OTf)]^+$ (**B0**) [see Figure 1b], as shown in Scheme 1, and is computed to be endothermic by 16.7 kcal/mol. In the subsequent step, intermediate **B0** reacts with the olefin substrate via transition state **TS0** to form intermediate **C**. The activation energy for this step is computed to be 19.5 kcal/mol, with respect to intermediate **B0**, and at a barrier of 36.2 kcal/mol from the CH_3CN-coordinated intermediate **B** in solvent phase (CH_3CN) at the B3LYP/TZVP//B3LYP/6-31G(d)-LANL2DZ level of theory. Transition state **TS0** exhibited a characteristic imaginary frequency of $i108$ cm^{-1} [see Figure 1c]. Subsequently, the alkene-coordinated intermediate **C** is formed from this dissociative pathway [**B** → **B0** → **TS0** → **C**] and this reaction is endothermic by 27.7 kcal/mol, with regard to intermediate **B**.

In the associative pathway, the olefin substrate directly attaches to intermediate **B** and form a five-membered transition state **TS1**, for which the activation barrier was estimated to be 44.9 kcal/mol in solvent phase (CH_3CN) at the B3LYP/TZVP//B3LYP/6-31G(d)-LANL2DZ level of theory. The transition state **TS1** exhibited a characteristic imaginary frequency of $i86$ cm^{-1}, corresponding to a significant increase of the distance between the Ni center and nitrogen (N7) of acetonitrile [Ni···N7 = 2.658 Å] when compared to that in starting intermediate **B** [1.890 Å], along with simultaneous shortening of the nickel and alkene distance [Ni···C9 = 2.747 Å and Ni···C10 = 3.030 Å]. Transition state **TS1** depicts the dissociation of CH_3CN and association of the alkene to the Ni center occurring synchronously and displayed a barrier height of 44.9 kcal/mol [see Figure 1d]. Note that, when transition state **TS1** was computed for the nickel N-heterocyclic carbene complexes bearing the ethyl and isopropyl substituents, as per in the experimental study,[8]

the barrier height remained unchanged [45.0 kcal/mol; see the Computational Details section, presented later in this work, for further discussion]. The approach of the alkene to the Ni center results in weaker Ni−(NHC) interactions, as reflected in the increased Ni−$C_{carbene}$ bond lengths in transition state **TS1** [Ni−C1 = 1.977 Å and Ni−C3 = 1.960 Å], with respect to that in the starting intermediate **B** [Ni−C1 = 1.959 Å and Ni−C3 = 1.953 Å]. Finally, the alkene-coordinated intermediate **C** is formed from this associative pathway [**B** → **TS1** → **C**] and this reaction is endothermic by 27.7 kcal/mol, with respect to intermediate **B**.

The asymmetrically bound alkene in intermediate **C** showed strong bonding interactions with the Ni center, as seen from the small interatomic Ni−C_{alkene} distances [Ni−C9 = 2.184 Å and Ni···C10 = 2.271 Å] [see Figure S2 in the Supporting Information]. The geometry of intermediate **C** is slightly distorted from a square planar structure, as the angles ∠C3−Ni−O1 and ∠C3−Ni−C9 are, respectively, 84.2° and 97.2°, instead of the expected value of 90°. The Ni−C_{olefin} bond dissociation energy (D_e) was estimated to be 20.8 kcal/mol in the acetonitrile solvent, as computed at the B3LYP/TZVP//B3LYP/6-31G(d)-LANL2DZ level of theory. The d/b ratio of 4.1 for the alkene-bound intermediate **C** is smaller than the acetonitrile-bound intermediate **B** [d/b = 6.07], and is a consequence of a greater π-back-bonding from the Ni center to the bound olefin moiety in intermediate **C**. The molecular orbital (MO) correlation diagram revealed that the $[(NHC)_2Ni(OTf)]^+$ (acceptor)−CH_2=CHCN (donor) interactions is comprised of donations from p-type orbitals of CH_2=CHCN moiety to the d-type FMOs of the $[(NHC)_2Ni(OTf)]^+$ fragment in intermediate **C** [see Figure S3 in the Supporting Information]. Between the dissociative and associative pathways, the calculations reveal that the dissociative pathway is kinetically preferred [see Figure 3].
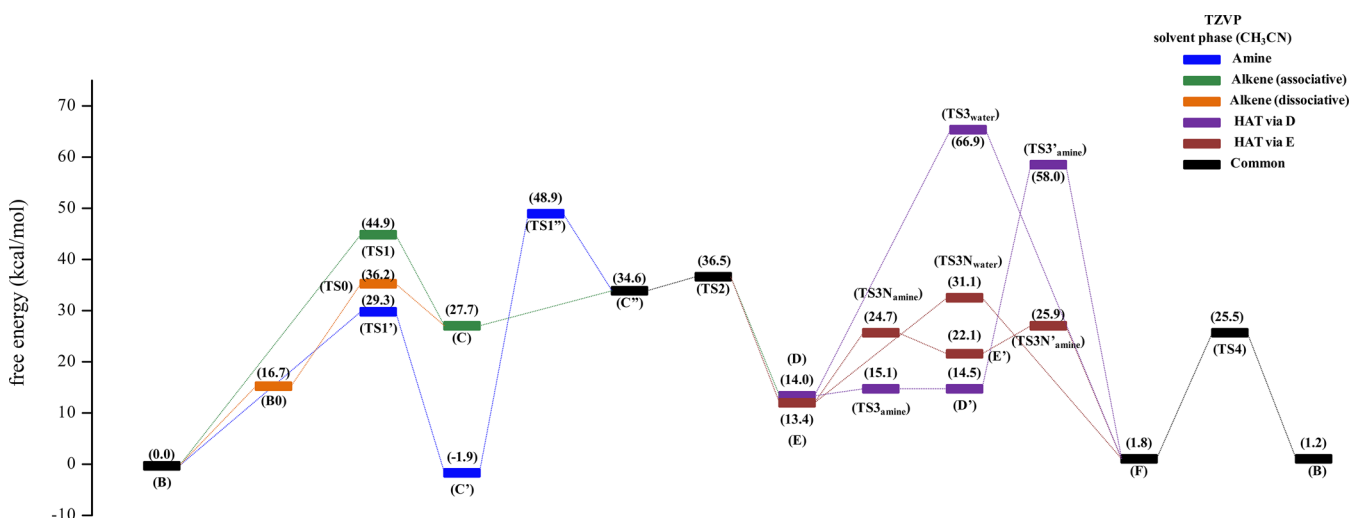
Figure 3. Overlay of the computed solvent (MeCN) phase free energies (ΔG) at the B3LYP/TZVP//B3LYP/6-31G(d)-LANL2DZ level of theory, depicting amine (blue) and alkene (green) coordination pathways for the hydroamination of acrylonitrile with dimethylamine, as catalyzed by a representative nickel N-heterocyclic carbene precatalyst (**A**) proceeding via a water/amine-mediated proton transfer step. Common pathways are given in black and hydrogen atom transfer (HAT) is shown in purple and brick red, via intermediates **D** and **E**, respectively.

Intermediate **C** further reacts with NHMe$_2$ to form the species $[(\text{NHC})_2\text{Ni}(\text{CH}(\text{NC})\text{CH}_2\text{NHMe}_2)(\text{OTf})]^+$ (**D**) via a transition state **TS2**. Our calculations reveal the presence of another intermediate $[(\text{NHC})_2\text{Ni}(\text{CNCH}=\text{CH}_2)(\text{OTf})]^+$ (**C″**), in which the amine interacts weakly with the alkene, on the way to the formation of transition state **TS2**. Note that this intermediate $[(\text{NHC})_2\text{Ni}(\text{CNCH}=\text{CH}_2)(\text{OTf})]^+$ (**C″**) is a common intermediate for both the associative [**B → TS1 → C → C″**] and the dissociative [**B → B0 → TS0 → C → C″**] pathways of the alkene coordination route, as discussed earlier, and also for the amine coordination route [**B → TS1′ → C′ → TS1″ → C″**], to be discussed next.

The coordination of NHMe$_2$ yields two resonance intermediates, i.e., the C-bound $[(\text{NHC})_2\text{Ni}(\text{CH}(\text{NC})\text{CH}_2\text{NHMe}_2)\text{-}(\text{OTf})]^+$ (**D**) and the N-bound $[(\text{NHC})_2\text{Ni}(\text{NCCHCH}_2\text{N}\text{-}\text{HMe}_2)(\text{OTf})]^+$ (**E**) via transition state **TS2**, which is common for both the alkene and amine coordination pathways. Transition state **TS2** exhibits an energy barrier of 8.8 kcal/mol in the solvent (CH$_3$CN) phase, relative to the previous intermediate **C** in the alkene coordination pathway. However, if we consider the energy requirement from the initiating species **B**, transition state **TS2** has an overall barrier of 36.5 kcal/mol. This step is energetically highest among all the feasible pathways computed and is the rate-determining step of the overall reaction.[12] Transition state **TS2** depicts an anti-Markovnikov-type addition of the incoming NHMe$_2$ substrate to the nickel-bound alkene moiety.[4] The approach of NHMe$_2$ toward the C9 carbon of alkene (CH$_2$=CHCN) in transition state **TS2** is apparent from the decrease in N8···C9 distance [2.500 Å] and a simultaneous increase in the Ni···C9 distance [2.558 Å], and is characterized by an imaginary frequency of i112 cm^1 [see Figure 1e]. The Ni−C$_{carbene}$ bonds in **TS2** are slightly less ionic in nature, with ca. 23% contribution arising from the nickel atomic orbitals and ca. 77% from the C$_{carbene}$ atomic orbitals.

Amine Coordination Pathway. This pathway initiates with the coordination of NHMe$_2$ to the Ni center of the active intermediate **B** via transition state **TS1′** with the elimination of CH$_3$CN molecule and yielding an amine-coordinated intermediate $[(\text{NHC})_2\text{Ni}(\text{NHMe}_2)(\text{OTf})]^+$ (**C′**). The amine coordination

step goes through an activation barrier of 29.3 kcal/mol via an intermediary transition state **TS1′**, where simultaneous dissociation of CH$_3$CN and association of NHMe$_2$ was observed. The transition state **TS1′** was characterized by an imaginary frequency of i110 cm^{-1} [see Figure 1f] and has a barrier height of 29.3 kcal/mol. In this transition state, an elongation of the nickel and acetonitrile nitrogen (N7) bond [Ni···N7 = 2.170 Å] is observed, compared to the reactive intermediate **B** [Ni−N7 = 1.890 Å], along with the simultaneous shortening of the nickel and amine nitrogen (N8) distance [Ni···N8 = 2.410 Å]. The approach of amine to the Ni center in transition state **TS1′** results in weaker interactions between the Ni−(NHC) bonds, as is evident from the increased Ni−C$_{carbene}$ bond lengths [Ni−C1 = 1.984 Å and Ni−C3 = 1.967 Å], in comparison to the reacting intermediate (**B**) [Ni−C1 = 1.959 Å and Ni−C3 = 1.953 Å]. However, the approach of NHMe$_2$ in transition state **TS1′** does not result in any significant change in the Ni−C$_{carbene}$ bond polarity that showed ca. 21% contributions from the nickel atomic orbitals and ca. 79% contributions from carbon atomic orbitals, similar to that in intermediate **B** [Ni(21.2%)−C1(78.7%) and Ni(21%)−C3(78.9%)].

Transition state **TS1′** undergoes elimination of CH$_3$CN and consequently forms an amine-coordinated intermediate $[(\text{NHC})_2\text{Ni}(\text{NHMe}_2)(\text{OTf})]^+$ (**C′**) in a step exothermic by 1.9 kcal/mol, relative to the previous intermediate **B**. The amine showed weaker bonding interactions with the Ni center in intermediate **C′** [Ni−N8 = 1.983] than observed in the preceding acetonitrile-bound intermediate **B** [Ni−N7 = 1.890] [see Figure S4 in the Supporting Information]. The solvent (CH$_3$CN)-phase bond dissociation energy (D_e) of the Ni−NHMe$_2$ (amine) bond was computed to be 51.5 kcal/mol at the B3LYP/TZVP//B3LYP/6-31G(d)-LANL2DZ level of theory. As a consequence of strong Ni−NHMe$_2$ bonding interactions, an increase in the Ni−C$_{carbene}$ bond lengths was observed for intermediate **C′** [Ni−C1 = 1.973 Å and Ni−C3 = 1.963 Å], relative to the previous acetonitrile-bound intermediate **B** [Ni−C1 = 1.959 Å and Ni−C3 = 1.953 Å]. The CDA analysis showed that the interaction between the Ni center and amine nitrogen (N8) is predominantly σ-type in nature, as observed from a high d/b ratio of 8.3. Also, the computed molecular orbital (MO)

correlation diagram for the $[(NHC)_2Ni(OTf)]^+$ (*acceptor*)–$NHMe_2$ (*donor*) bond exhibited donations from σ-type FMOs of the $NHMe_2$ moiety to the *d*-type FMOs of the $[(NHC)_2Ni(OTf)]^+$ fragment in intermediate **C′** [see Figure S5 in the Supporting Information].

Intermediate **C′** undergoes an addition of $CH_2=CHCN$ to the Ni center, eliminating $NHMe_2$ to form the intermediate $[(NHC)_2Ni(CNCH=CH_2)(OTf)]^+$ (**C″**) via intermediary transition state **TS1″**. The approach of $CH_2=CHCN$ toward the Ni center in transition state **TS1″** is characterized by an imaginary frequency of $i85$ cm^{-1}. The transition state **TS1″** portrays a displacement along the Ni–C9 and Ni–N8 vectors, resulting in the simultaneous inward movement of $CH_2=CHCN$ and the outward movement of $NHMe_2$ from the metal center [see Figure 1g]. Transition state **TS1″** has a barrier height of 50.8 kcal/mol in the solvent (CH_3CN) phase, with respect to the previous intermediate **C′**. Transition state **TS1″** results in the formation of $CNCH=CH_2$ bound to the Ni center in intermediate **C″** [see Figure S6 in the Supporting Information] and is marked by the attack of $NHMe_2$ on the metal-bound olefin moiety. The alkene-coordinated intermediate **C″** is 36.5 kcal/mol endothermic, relative to the previous intermediate **C′**. Similar to the alkene coordination route, the amine coordination route may proceed via dissociative and associative pathways. However, here, in the amine coordination route, we have restricted our calculations to the associative pathway and this is due to the fact that the rate-determining step is **TS1″** and, therefore, calculations for the dissociative pathway are not required.

Intermediate **C″** undergoes an anti-Markovnikov-type attack of $NHMe_2$ on the metal-bound olefin moiety in transition state **TS2**, resulting in the formation of the resonance intermediates, i.e., the C-bound $[(NHC)_2Ni(CH(CN)CH_2NHMe_2)(OTf)]^+$ (**D**) and the N-bound $[(NHC)_2Ni(NCCHCH_2NHMe_2)(OTf)]^+$ (**E**). This step is exothermic, by 20.6 and 21.2 kcal/mol, with respect to the intermediate **C″**. Similar anti-Markovnikov-type hydroamination reaction has been noted for a rhodium complex.[4] The C-bound intermediate **D** showed strong binding between the Ni center and the alkylamine moiety with the Ni–C10 bond length of 2.009 Å [see Figure S7 in the Supporting Information] and exhibited a high bond dissociation energy (D_e) of 81.6 kcal/mol computed in the solvent (CH_3CN) phase at the B3LYP/TZVP//B3LYP/6-31G(d)-LANL2DZ level of theory. The Ni–C10 bonding interaction was found to be predominantly σ-bonding with a *d/b* ratio of 6.9. The MO correlation diagram revealed that the $[(NHC)_2Ni(OTf)]^+$ (*acceptor*)–$CH(CN)CH_2NHMe_2$ (*donor*) interaction was comprised of donations from σ-type FMOs of the $CNCHCH_2NHMe_2$ moiety to the *d*-type FMOs of the $[(NHC)_2Ni(OTf)]^+$ fragment [see Figure S8 in the Supporting Information]. The N-bound intermediate **E** is 0.6 kcal/mol more stable, compared to the C-bound intermediate **D**, and exhibits a short Ni–N9 bond (Ni–N9 = 1.882 Å) [see Figure S9 in the Supporting Information]. Since this energy difference is comparable, both the C-bound intermediate **D** and the N-bound intermediate **E** have equal probability of proceeding further in the reaction. However, the kinetics in the proceeding step would dictate the preferred pathway.

The C-bound intermediate **D** and the N-bound intermediate **E** undergo a 1,3-proton transfer between an amine N8 to alkene carbon C10 assisted by a proton relay mechanism. This 1,3-proton transfer step invokes the presence of either an adventitious H_2O molecule or the unreacted $NHMe_2$ molecules. The prospects of these two possibilities are discussed below.

Water-Assisted Proton Relay. The water-assisted proton relay displays an activation barrier of 52.9 kcal/mol with respect to the C-bound intermediate **D** and 17.7 kcal/mol, with respect to intermediate **E** through the formation of six-membered transition states **TS3$_{water}$** and **TS3N$_{water}$**, respectively. The barrier height of the water-assisted hydrogen atom transfer (HAT) via the intermediates **D** and **E** provides a clear picture about the formation of intermediate **F**. In this regard, the direct proton transfer through the four-membered transition state **TS3** displayed a slightly higher barrier height of 54.3 kcal/mol [see Figure S10 in the Supporting Information]. Transition state **TS3$_{water}$** was verified by a characteristic imaginary frequency of $i1542$ cm^{-1}, corresponding to the proton transfer occurring between C10···H2 (water hydrogen) ···O4 (water oxygen) and O4···H1 (amine hydrogen) ···N8, and stretching along the Ni···C10 [2.425 Å] bond [see Figure 1h], which subsequently results in the formation of intermediate $[(NHC)_2Ni(NCCH_2CH_2NMe_2)(OTf)]^+$ (**F**) having Ni–N9 (nitrile nitrogen of the $CNCH_2CH_2NMe_2$ moiety) coordination. Similarly, transition state **TS3N$_{water}$** was verified by a characteristic imaginary frequency of $i1476$ cm^{-1}, corresponding to the proton transfer occurring between C10···H2 (water hydrogen) ···O4 (water oxygen) and O4···H1 (amine hydrogen) ···N8, and stretching along the Ni···N9 [1.878 Å] bond [see Figure 1i], yielding the same intermediate **F**.

Amine-Assisted Proton Transfer. Apart from water, we have also explored the possibility of a proton shuttle mechanism assisted by the unreacted amine substrate molecules. The amine-assisted proton relay is proposed to proceed in a two-step fashion, because of the bulkiness of the methyl groups present. Thus, the first step of the amine-assisted relay involves proton transfer from an amine N8 in the C-bound intermediate **D** and N-bound intermediate **E** to N10 of $NHMe_2$, yielding transition states **TS3$_{amine}$** and **TS3N$_{amine}$**, respectively, which displays an activation barrier of 1.1 kcal/mol, with respect to the C-bound intermediate **D** for transition state **TS3$_{amine}$** and 11.3 kcal/mol with respect to the N-bound intermediate **E** for transition state **TS3N$_{amine}$**. Transition state **TS3$_{amine}$** was verified by a characteristic imaginary frequency of $i1011$ cm^{-1}, depicting a displacement vector in the direction of hydrogen transfer from N9 to N10 of $NHMe_2$ [see Figure 1j]. Similarly, the transition state **TS3N$_{amine}$** displayed an imaginary frequency of $i856$ cm^{-1} [see Figure 1k]. The transition states, **TS3$_{amine}$** and **TS3N$_{amine}$**, yield ammonium ion $[(NH_2(CH_3)_2]^+$-bound intermediates, $[(NHC)_2Ni(CH(CN)CH_2NMe_2)(OTf)][(NH_2(CH_3)_2]^+$ (**D′**) and $[(NHC)_2Ni(NCCHCH_2NMe_2)(OTf)][(NH_2Me_2]^+$ (**E′**) [see Figures S11 and S12 in the Supporting Information]. The formation of the resonance intermediates, the C-bound intermediate **D′** and N-bound intermediate **E′**, are endothermic by 14.5 and 22.1 kcal/mol, with respect to the initial intermediate **B**, respectively.

Intermediates **D′** and **E′** subsequently undergo another intermolecular proton transfer from the ammonium nitrogen N10 to alkene carbon C10 to form an enamine-bound cationic intermediate **F** via the transition states **TS3′$_{amine}$** and **TS3N′$_{amine}$**, respectively. As expected, transition states **TS3′$_{amine}$** and **TS3N′$_{amine}$** exhibited imaginary frequencies of $i1152$ cm^{-1} and $i488$ cm^{-1} [see Figures 1l and 1m] along the displacement vectors in the direction of hydrogen atom transfer from ammonium N10 to C10 atoms and exhibited corresponding activation barriers of 43.5 and 3.8 kcal/mol, with respect to

intermediates D' and E', respectively. A very large barrier height is noted for transition state $TS3'_{amine}$, as a result of the cleavage of a rather strong Ni−C bond, leading to the formation of a three-coordinated Ni(II) species. The energetics of the computed pathways favor the proton transfer occurring via the N-bound intermediate E, instead of the C-bound intermediate D for both of the water-assisted and the amine-assisted pathways. It is important to note that the amine-assisted paths significantly bring down the activation barrier of the 1,3-proton transfer step of the hydroamination reaction [see Figure S13 in the Supporting Information].[4]

Both transition states—$TS3N_{water}$, in the case of the water-assisted proton relay, and $TS3N'_{amine}$, in the case of the amine-assisted proton relay—lead to intermediate F. It showed a strong bonding interaction between the Ni center and N9 (nitrile nitrogen), as evident from a short Ni−N9 bond length [1.887 Å] [see Figure S14 in the Supporting Information] and is in good agreement with the sum of individual covalent radii of Ni and N atoms [1.81 Å].[11] Intermediate F is exothermic by 12.2 kcal/mol, with respect to the previous intermediate D. The Ni−N9 bond was found to be predominantly σ-bonding in nature exhibiting a d/b ratio of 6.8. The solvent-phase Ni−N9 bond dissociation energy (D_e) in acetonitrile was found to be 47.5 kcal/mol, as computed at the B3LYP/TZVP//B3LYP/6-31G(d)-LANL2DZ level of theory [see Figure S15 in the Supporting Information]. Lastly, the NBO analysis revealed that the Ni−N9 bond is highly ionic in nature, with orbital contributions from nickel-based atomic orbitals being ~13% while nitrogen (N9)-based atomic orbitals contributing the remaining 86%. The MO correlation diagram showed bonding interaction between the $[(NHC)_2Ni(OTf)]^+$ (*acceptor*) and $NCCH_2CH_2NMe_2$ (*donor*) fragments, comprised of σ-type donations from the FMOs of the $NCCH_2CH_2NMe_2$ (*donor*) moiety to the d-type FMOs of the $[(NHC)_2Ni(OTf)]^+$ fragment.

Intermediate F, upon the addition of CH_3CN, gives back the initiating species B via transition state $TS4$, with the elimination of the product molecule ($NCCH_2CH_2NMe_2$). Transition state $TS4$ exhibited an energy barrier of 23.7 kcal/mol, with respect to intermediate F, and which was characterized by the imaginary frequency of $i98$ cm^{-1} along the displacement vector in the direction of Ni−N7 (acetonitrile nitrogen) [2.269 Å] bond formation and the Ni−N9 [2.168 Å] bond dissociation [see Figure 1n]. In the overall, hydroamination reaction was found to be almost thermoneutral.

Alkene versus Amine Coordination Pathway. An overlay of the free-energy profiles of the different possibilities explored, i.e., associative alkene coordination [$B \rightarrow TS1 \rightarrow C \rightarrow C''$] pathway, dissociative alkene coordination [$B \rightarrow B0 \rightarrow TS0 \rightarrow C \rightarrow C''$] pathway, and amine coordination [$B \rightarrow TS1' \rightarrow C' \rightarrow TS1'' \rightarrow C''$] pathway, is shown in Figure 3. The proposed catalytic cycle for the hydroamination reaction has been investigated for the alkene and the amine coordination pathways. The two routes follow different energetics until reaching a common intermediate C'', after which they merge into a single pathway. The amine coordination route first initiates with the coordination of an amine ($NHMe_2$) to the active intermediate species B, followed by the addition of the olefin (CH_2=$CHCN$) substrate. This yields the resonance intermediates, the C-bound intermediate D and N-bound intermediate E species via transition state $TS2$. Similarly, the alkene coordination route may proceed by an associative and a dissociative pathway, which involves the addition of an alkene

(CH_2=$CHCN$) followed by the amine coordination leading to the resonance intermediates, D and E, via transition state $TS2$.

The first transition states for both the pathways, i.e., $TS1$ and $TS1'$, have a significant difference between their activation energies. Transition state $TS1$ showed an activation energy barrier of 44.9 kcal/mol, while the transition state $TS1'$ had a much lower barrier of 29.3 kcal/mol. This difference in energy implies that the binding of amine ($NHMe_2$) to the Ni center in $TS1'$ is more favorable, compared to the binding of alkene (CH_2=$CHCN$) to that of nickel in $TS1$. Transition states $TS1$ and $TS1'$ result in intermediates C and C', respectively. The alkene (CH_2=$CHCN$)-coordinated intermediate C is endothermic by 27.7 kcal/mol, while the amine ($NHMe_2$)-coordinated intermediate C' is exothermic by 1.9 kcal/mol, with respect to the preceding intermediate B. This difference in energy of 29.6 kcal/mol between intermediates C and C' is significantly large, indicating the relative stability that arises as a result of amine coordination to the Ni center, compared to the alkene coordination. Also, the bond dissociation energy of Ni−N9 (amine nitrogen) of 51.5 kcal/mol is more than double that of the Ni−C_{alkene} bond [20.8 kcal/mol], and this is attributed to more effective σ-bonding between the Ni−N9 (amine nitrogen) in C' with a higher d/b ratio of 8.3, compared to the Ni−C_{alkene} bonding in C having a lower d/b ratio of 4.1.

Intermediate C in the alkene coordination pathway directly leads to the resonance intermediates D and E, via transition state $TS2$. While in the amine coordination pathway, intermediate C' goes via intermediate C'', which then proceeds to the formation of the resonance intermediates D and E, via transition state $TS2$. In this regard, note that transition state $TS0$ of the CH_3CN dissociation in the alkene coordination pathway, and transition state $TS2$, which is common for both the alkene coordination and amine coordination routes, are equally competitive and either of them can represent the rate-determining step of the alkene hydroamination reaction. Overall, the alkene coordination pathway is the minimum energy pathway and is favorable over the amine coordination pathway, despite the fact that the initial alkene coordination step is higher in energy.

■ CONCLUSIONS

In summary, the mechanism for the hydroamination reaction of vinyl nitrile (CH_2=$CHCN$) with dimethylamine ($NHMe_2$), as catalyzed by a nickel(II) N-heterocyclic carbene complex, namely, *trans*-[1,4-dimethyl-1,2,4-triazol-5-ylidene]$_2$NiCl$_2$, has been studied using density functional theory (DFT). Two possible mechanistic pathways for this reaction are explored, namely, (i) the alkene coordination pathway, and (ii) the amine coordination pathway. Within these two pathways, several possible scenarios involving associative and dissociative mechanisms are explored. The pathway with the least energy penalty is summarized in Figure 4. Our calculations categorically suggest that the reaction proceeds via the alkene coordination pathway, because the energetic cost associated with amine coordination pathway is relatively higher. Of particular interest is the fact that both of these two pathways converge at a common intermediate state C'', and then proceed along a common route. Our calculated barrier heights suggest that the overall rate-determining step of the reaction is dependent on the coordination of the alkene to the metal center, as depicted by transition state $TS0$, and also upon the amine attacking the metal coordinated alkene species, as designated by transition state $TS2$. Lastly, the presence of
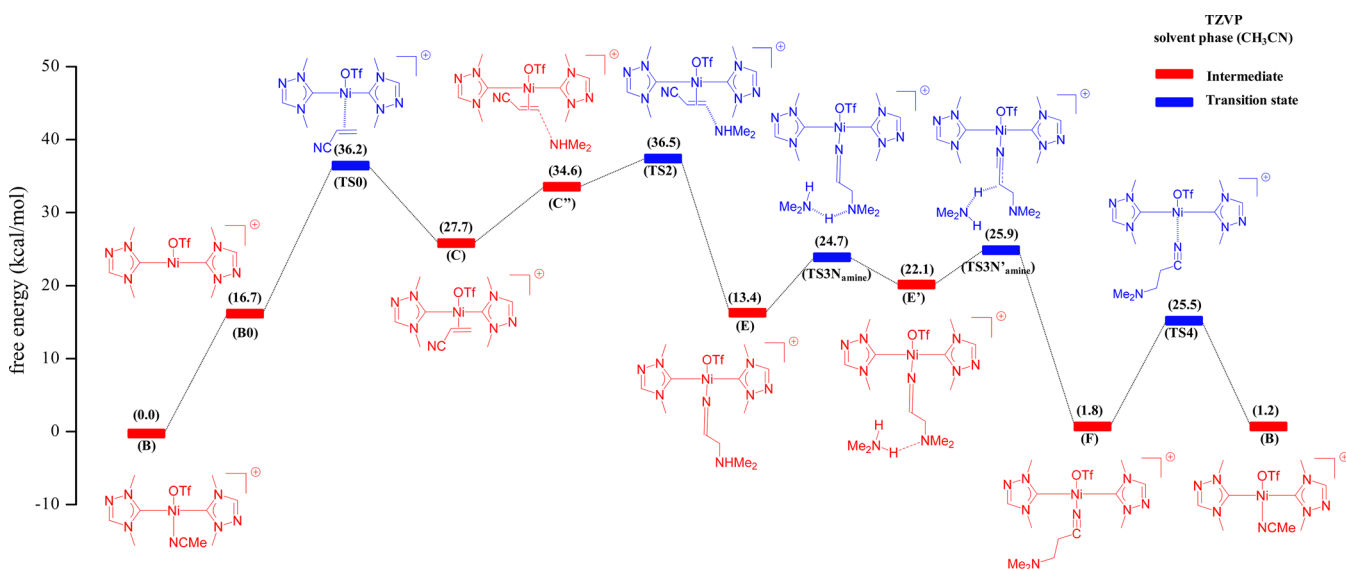
Figure 4. Overlay of the computed solvent (MeCN)-phase free energies (ΔG) at the B3LYP/TZVP//B3LYP/6-31G(d)-LANL2DZ level of theory, depicting the overall hydroamination of acrylonitrile with dimethylamine as catalyzed by a representative Ni N-heterocyclic carbene precatalyst (**A**), proceeding via an amine-mediated proton transfer.

adventitious water molecules or of the unreacted amine substrate molecules in the reaction mixture play a crucial role in a 1,3-proton transfer step by significantly lowering the activation barrier. This implies that the explicit stabilization of the microsolvated transition state leading to the facile proton transfer between N9 and C10 atoms facilitates the overall alkene hydroamination reaction. From our results, we infer that the lowest energy pathway proceeds via the alkene coordination route, followed by the amine (NHMe$_2$)-assisted 1,3-proton shuttle proceeding via the N-bound intermediate **E**. The critical role played by the 1,3-proton transfer step in the alkene hydroamination reaction is similar to the alkyne hydroamination reaction that we observed earlier.[10]

■ COMPUTATIONAL METHODS

Density functional theory (DFT) calculations were performed on the reactant, product, transition states, and the intermediates using the GAUSSIAN 09 suite[13] of quantum chemical programs. In particular, the DFT calculations were performed on the stationary points (**B**–**F**, **C′**–**C″**) and the transition states (**TS1**–**TS4, TS1′**–**TS1″**) of the proposed mechanistic cycle. The Becke three-parameter exchange functional, in conjunction with the Lee–Yang–Parr correlation functional (B3LYP), has been employed in the study.[14] The 6-31G(d)[15] basis set was used to describe O, S, F, C, N, and H atoms, while the LANL2DZ basis set was used for the Ni atom.[16] Finally, higher-level single-point calculations on the stationary points (**B**–**F**, **C′**–**C″**) and the transition states (**TS1**–**TS4, TS1′**–**TS1″**) of the proposed mechanistic cycle were performed on the respective B3LYP/6-31G(d)-LANL2DZ optimized geometries, using the TZVP basis set for all atoms (B3LYP/TZVP//B3LYP/6-31G(d)-LANL2DZ).[17] In addition, to check the basis set dependence on the calculations, geometry optimizations were also performed on selected species, using B3LYP and 6-31G(d) basis set for all atoms. These geometries were then utilized to perform single-point calculations using TZVP for all atoms (B3LYP/TZVP//B3LYP/6-31G(d)). We observed only marginal differences in computed energetics [see Table S30 in the Supporting Information], and this offers confidence in the employed methodology. Calculations were performed on the model system ({1,4-dimethyl-1,2,4-triazol-5-ylidene]$_2$Ni(NCCH$_3$)(OTf)}$^+$), where the ethyl and isopropyl groups in 1,4-positions are substituted using the methyl group, for simplicity. However, to see the effect of the substituents on the computed energetics, we have also performed

additional calculations employing the original substituents, which yield only a marginal reduction in the barrier heights [see Table S44 and Figures S16–S23 in the Supporting Information]. In addition, we have also explored a dissociative pathway for **E′** to **F** conversion where the counteranion OTf is expected to dissociate; however, this pathway found to yield a larger kinetic barrier and, therefore, has not been discussed further [see Table S45 and Figures S24–S26 in the Supporting Information]. Natural bond orbital (NBO) analysis[18] was performed using the NBO 3.1 program implemented in the GAUSSIAN 09 package. The transition state (TS) optimization method based on the Berny algorithm was used for the transition-state optimizations.[19] Frequency calculations were performed for all of the optimized structures, to characterize the stationary points as minima and the transition states as maxima. The solvation energy has been incorporated using the Polarizable Continuum Model (PCM)[20] with acetonitrile solvent via single-point energy calculations of the optimized gas-phase geometries. All the energy values discussed are the solvation-corrected free energies in acetonitrile, unless otherwise stated. The metal–ligand *donor–acceptor* interactions were inspected by using the charge decomposition analysis (CDA),[21] which is a valuable tool for analyzing the interactions between molecular fragments on a quantitative basis, with an emphasis on the electron donation.[22] The *donor–acceptor* interactions were examined using this technique for the various stationary points **B**–**F** and **C′**–**C″** of the proposed catalytic cycle. The orbital interaction between a donor and an acceptor fragments [*acceptor* = [(NHC)$_2$Ni(OTf)]$^+$ in (**B**–**F**), while *donor* = CH$_3$CN in **B**, CH$_2$=CHCN in **C**, NHMe$_2$ in **C′**, CNCH = CH$_2$···NHMe$_2$ in **C″**, C-bound CH(CN)CH$_2$NHMe$_2$ in **D**, and N-bound NCCH$_2$CH$_2$NMe$_2$ in **F**] can be divided into three parts:

(i) σ-donation from the (*donor*) → (*acceptor*) fragment (*d*);

(ii) *p*-back-donation from the (*donor*) ← (*acceptor*) fragment (*b*); and

(iii) a repulsive interaction (*r*) between the occupied molecular orbitals (MOs) of these two fragments.

The CDA calculations were performed using the AOMix[23] program with the B3LYP/6-31G(d)-LANL2DZ wave function. Molecular orbital (MO) compositions and the overlap populations were calculated using the AOMix program. Analysis of the MO compositions, in terms of occupied and unoccupied fragment orbitals (OFOs and UFOs, respectively), construction of orbital interaction diagrams, the charge decomposition analysis (CDA) were performed using the AOMix-CDA.[24]

ASSOCIATED CONTENT

Supporting Information

The Supporting Information is available free of charge on the ACS Publications website at DOI: 10.1021/acs.inorgchem.7b02097.

> Molecular geometries and electronic energies of all species (PDF)

AUTHOR INFORMATION

Corresponding Authors

*Fax: +91-22-2572-3480. E-mail: rajaraman@chem.iitb.ac.in (G. Rajaraman).

*Fax: +91-22-2572-3480. E-mail: pghosh@chem.iitb.ac.in (P. Ghosh).

ORCID

Gopalan Rajaraman: 0000-0001-6133-3026

Prasenjit Ghosh: 0000-0002-9479-8177

Author Contributions

†These authors contributed equally to this manuscript.

Notes

The authors declare no competing financial interest.

ACKNOWLEDGMENTS

REFERENCES

(1) (a) Muller, T. E.; Hultzsch, K. C.; Yus, M.; Foubelo, F.; Tada, M. Hydroamination: direct addition of amines to alkenes and alkynes. *Chem. Rev.* **2008**, *108*, 3795−3892. (b) Villa, M.; Jacobi von Wangelin, A. Hydroaminations of alkenes: a radical, revised, and expanded version. *Angew. Chem., Int. Ed.* **2015**, *54*, 11906−11908. (c) Zi, G. Asymmetric hydroamination/cyclization catalyzed by organolanthanide complexes with chiral biaryl-based ligands. *Dalton Trans.* **2009**, 9101−9109.

(2) (a) Cao, P.; Cabrera, J.; Padilla, R.; Serra, D.; Rominger, F.; Limbach, M. Hydroamination of Unactivated Alkenes Catalyzed by Novel Platinum (II) N-Heterocyclic Carbene Complexes. *Organometallics* **2012**, *31*, 921−929. (b) Chemler, S. R. The enantioselective intramolecular aminative functionalization of unactivated alkenes, dienes, allenes and alkynes for the synthesis of chiral nitrogen heterocycles. *Org. Biomol. Chem.* **2009**, *7*, 3009−3019. (c) Hesp, K. D.; Stradiotto, M. Rhodium-and Iridium-Catalyzed Hydroamination of Alkenes. *ChemCatChem* **2010**, *2*, 1192−1207. (d) Lepori, C.; Hannedouche, J. First-Row Late Transition Metals for Catalytic (Formal) Hydroamination of Unactivated Alkenes. *Synthesis* **2017**, *49*, 1158−1167. (e) Brill, M.; Nahra, F.; Gómez-Herrera, A.; Zinser, C.; Cordes, D. B.; Slawin, A. M.; Nolan, S. P. Gold-N-Heterocyclic Carbene Complexes of Mineral Acids. *ChemCatChem* **2017**, *9*, 117−120. (f) Lavallo, V.; Frey, G. D.; Donnadieu, B.; Soleilhavoup, M.; Bertrand, G. Homogeneous catalytic hydroamination of alkynes and allenes with ammonia. *Angew. Chem., Int. Ed.* **2008**, *47*, 5224−5228. (g) Zeng, X.; Soleilhavoup, M.; Bertrand, G. Gold-catalyzed intermolecular Markovnikov hydroamination of allenes with secondary amines. *Org. Lett.* **2009**, *11*, 3166−3169. (h) Kinjo, R.; Donnadieu, B.; Bertrand, G. Gold-Catalyzed Hydroamination of Alkynes and Allenes with Parent Hydrazine. *Angew. Chem., Int. Ed.* **2011**, *50*, 5560−5563. (i) López-Gómez, M. J.; Martin, D.; Bertrand, G. Anti-Bredt N-heterocyclic carbene: an efficient ligand for the gold(I)-catalyzed hydroamination of terminal alkynes with parent hydrazine. *Chem. Commun.* **2013**, *49*, 4483−4485. (j) Hu, X.; Martin, D.; Bertrand, G.

Room temperature hydroamination of alkynes with anilines catalyzed by anti-Bredt di(amino)carbene gold(I) complexes. *New J. Chem.* **2016**, *40*, 5993−5996.

(3) Straub, T.; Haskel, A.; Neyroud, T. G.; Kapon, M.; Botoshansky, M.; Eisen, M. S. Intermolecular hydroamination of terminal alkynes catalyzed by organoactinide complexes. Scope and mechanistic studies. *Organometallics* **2001**, *20*, 5017−5035.

(4) Couce-Rios, A.; Lledós, A.; Ujaque, G. The Origin of Anti-Markovnikov Regioselectivity in Alkene Hydroamination Reactions Catalyzed by [Rh (DPEphos)]⁺. *Chem.—Eur. J.* **2016**, *22*, 9311−9320.

(5) (a) Aullón, G.; Gómez, K.; González, G.; Jansat, S.; Martínez, M.; Poli, R.; Rodríguez-Zubiri, M. Kinetico-Mechanistic Information about Alkene Hydroamination with Aniline in Bromide-Rich Ionic Media: Importance of Solvolysis. *Inorg. Chem.* **2011**, *50*, 5628−5636. (b) Liu, Z.; Yamamichi, H.; Madrahimov, S. T.; Hartwig, J. F. Rhodium Phosphine−π-Arene Intermediates in the Hydroamination of Alkenes. *J. Am. Chem. Soc.* **2011**, *133*, 2772−2782. (c) Wang, C.; Ren, X.-R.; Qi, C.-Z.; Yu, H.-Z. Mechanistic Study on Gold-Catalyzed Highly Selective Hydroamination of Alkylidenecyclopropanes. *J. Org. Chem.* **2016**, *81*, 7326−7335.

(6) (a) Ramasamy, B.; Ghosh, P. The Developing Concept of Bifunctional Catalysis with Transition Metal N-Heterocyclic Carbene Complexes. *Eur. J. Inorg. Chem.* **2016**, *2016*, 1448−1465. (b) Prakasham, A.; Ghosh, P. Nickel N-heterocyclic carbene complexes and their utility in homogeneous catalysis. *Inorg. Chim. Acta* **2015**, *431*, 61−100. (c) Kumar, A.; Ghosh, P. Studies of the Electronic Properties of N-Heterocyclic Carbene Ligands in the Context of Homogeneous Catalysis and Bioorganometallic Chemistry. *Eur. J. Inorg. Chem.* **2012**, *2012*, 3955−3969. (d) John, A.; Ghosh, P. Fascinating frontiers of N/O-functionalized N-heterocyclic carbene chemistry: from chemical catalysis to biomedical applications. *Dalton Trans.* **2010**, *39*, 7183−7206. (e) Huang, L.; Arndt, M.; Gooßen, K.; Heydt, H.; Gooßen, L. J. Late transition metal-catalyzed hydroamination and hydroamidation. *Chem. Rev.* **2015**, *115*, 2596−2697. (f) Ritleng, V.; Henrion, M. l.; Chetcuti, M. J. Nickel N-Heterocyclic Carbene-Catalyzed C−Heteroatom Bond Formation, Reduction, and Oxidation: Reactions and Mechanistic Aspects. *ACS Catal.* **2016**, *6*, 890−906. (g) Pirnot, M. T.; Wang, Y. M.; Buchwald, S. L. Copper hydride catalyzed hydroamination of alkenes and alkynes. *Angew. Chem., Int. Ed.* **2016**, *55*, 48−57. (h) Fernández-Salas, J. A.; Marelli, E.; Cordes, D. B.; Slawin, A. M.; Nolan, S. P. General and Mild Ni⁰-Catalyzed α-Arylation of Ketones Using Aryl Chlorides. *Chem.—Eur. J.* **2015**, *21*, 3906−3909. (i) Jacobsen, H.; Correa, A.; Poater, A.; Costabile, C.; Cavallo, L. Understanding the M (NHC)(NHC= N-heterocyclic carbene) bond. *Coord. Chem. Rev.* **2009**, *253*, 687−703.

(7) (a) Ray, S.; Asthana, J.; Tanski, J. M.; Shaikh, M. M.; Panda, D.; Ghosh, P. Design of nickel chelates of tetradentate N-heterocyclic carbenes with subdued cytotoxicity. *J. Organomet. Chem.* **2009**, *694*, 2328−2335. (b) Ray, S.; Mohan, R.; Singh, J. K.; Samantaray, M. K.; Shaikh, M. M.; Panda, D.; Ghosh, P. Anticancer and antimicrobial metallopharmaceutical agents based on palladium, gold, and silver N-heterocyclic carbene complexes. *J. Am. Chem. Soc.* **2007**, *129*, 15042−15053.

(8) Dash, C.; Shaikh, M. M.; Butcher, R. J.; Ghosh, P. A comparison between nickel and palladium precatalysts of 1,2,4-triazole based N-heterocyclic carbenes in hydroamination of activated olefins. *Dalton Trans.* **2010**, *39*, 2515−2524.

(9) Dash, C.; Shaikh, M. M.; Butcher, R. J.; Ghosh, P. Highly convenient regioselective intermolecular hydroamination of alkynes yielding ketimines catalyzed by gold(I) complexes of 1,2,4-triazole based N-heterocyclic carbenes. *Inorg. Chem.* **2010**, *49*, 4972−4983.

(10) Katari, M.; Rao, M. N.; Rajaraman, G.; Ghosh, P. Computational insight into a gold(I) N-heterocyclic carbene mediated alkyne hydroamination reaction. *Inorg. Chem.* **2012**, *51*, 5593−5604.

(11) Cordero, B.; Gómez, V.; Platero-Prats, A. E.; Revés, M.; Echeverría, J.; Cremades, E.; Barragán, F.; Alvarez, S. Covalent radii revisited. *Dalton Trans.* **2008**, 2832−2838.

(12) (a) Yagisawa, S. Two types of rate-determining step in chemical and biochemical processes. *Biochem. J.* **1989**, *263*, 985−988.

(b) Kozuch, S.; Shaik, S. How to conceptualize catalytic cycles? The energetic span model. *Acc. Chem. Res.* **2011**, *44*, 101−110.

(13) Frisch, M. J.; Trucks, G. W.; Schlegel, H. B.; Scuseria, G. E.; Robb, M. A.; Cheeseman, J. R.; Scalmani, G.; Barone, V.; Mennucci, B.; Petersson, G. A.; Nakatsuji, H.; Caricato, M.; Li, X.; Hratchian, H. P.; Izmaylov, A. F.; Bloino, J.; Zheng, G.; Sonnenberg, J. L.; Hada, M.; Ehara, M.; Toyota, K.; Fukuda, R.; Hasegawa, J.; Ishida, M.; Nakajima, T.; Honda, Y.; Kitao, O.; Nakai, H.; Vreven, T.; Montgomery, J. A., Jr.; Peralta, J. E.; Ogliaro, F.; Bearpark, M.; Heyd, J. J.; Brothers, E.; Kudin, K. N.; Staroverov, V. N.; Kobayashi, R.; Normand, J.; Raghavachari, K.; Rendell, A.; Burant, J. C.; Iyengar, S. S.; Tomasi, J.; Cossi, M.; Rega, N.; Millam, J. M.; Klene, M.; Knox, J. E.; Cross, J. B.; Bakken, V.; Adamo, C.; Jaramillo, J.; Gomperts, R.; Stratmann, R. E.; Yazyev, O.; Austin, A. J.; Cammi, R.; Pomelli, C.; Ochterski, J. W.; Martin, R. L.; Morokuma, K.; Zakrzewski, V. G.; Voth, G. A.; Salvador, P.; Dannenberg, J. J.; Dapprich, S.; Daniels, A. D.; Farkas, Ö.; Foresman, J. B.; Ortiz, J. V.; Cioslowski, J.; Fox, D. J. *Gaussian 09*, revision A.02; Gaussian, Inc.: Wallingford, CT, 2009.

(14) (a) Perdew, J. P. Erratum: Density-functional approximation for the correlation energy of the inhomogeneous electron gas. *Phys. Rev. B: Condens. Matter Mater. Phys.* **1986**, *34*, 7406. (b) Becke, A. D. Density-functional exchange-energy approximation with correct asymptotic behavior. *Phys. Rev. A: At., Mol., Opt. Phys.* **1988**, *38*, 3098. (c) Lee, C.; Yang, W.; Parr, R. G. Development of the Colle-Salvetti correlation-energy formula into a functional of the electron density. *Phys. Rev. B: Condens. Matter Mater. Phys.* **1988**, *37*, 785.

(15) (a) Petersson, G.; Al-Laham, M. A. A complete basis set model chemistry. II. Open-shell systems and the total energies of the first-row atoms. *J. Chem. Phys.* **1991**, *94*, 6081−6090. (b) Petersson, a.; Bennett, A.; Tensfeldt, T. G.; Al-Laham, M. A.; Shirley, W. A.; Mantzaris, J. A complete basis set model chemistry. I. The total energies of closed-shell atoms and hydrides of the first-row elements. *J. Chem. Phys.* **1988**, *89*, 2193−2218. (c) Hehre, W. J.; Ditchfield, R.; Pople, J. A. Self-consistent molecular orbital methods. XII. Further extensions of Gaussian-type basis sets for use in molecular orbital studies of organic molecules. *J. Chem. Phys.* **1972**, *56*, 2257−2261.

(16) (a) Cárdenas-Jirón, G. I.; Gonzalez, C.; Benavides, J. Nitric Oxide Oxidation Mediated by Substituted Nickel Phthalocyanines: A Theoretical Viewpoint. *J. Phys. Chem. C* **2012**, *116*, 16979−16984. (b) Gutierrez, O.; Tantillo, D. J. Transition Metal Intervention for a Classic Reaction: Assessing the Feasibility of Nickel (0)-Promoted [1, 3] Sigmatropic Shifts of Bicyclo[3.2.0]hept-2-enes. *Organometallics* **2010**, *29*, 3541−3545. (c) Ishida, M.; Naruta, Y.; Tani, F. Copper (II) and nickel (II) hexafluorophosphate complexes derived from a monoanionic porphyrin analogue: Solvato-and thermochromism of the Ni complexes by spin-interconversion. *Dalton Trans.* **2010**, *39*, 2651−2659. (d) Das, O.; Adarsh, N.; Paul, A.; Paine, T. K. Copper (II) and nickel (II) complexes of β-aminoketoxime ligand: Syntheses, crystal structures, magnetism, and nickel (II) templated coupling of oxime with nitrile. *Inorg. Chem.* **2010**, *49*, 541−551. (e) Zhang, X.; Liu, B.; Liu, A.; Xie, W.; Chen, W. Steric Bulkiness-Dependent Structural Diversity in Nickel(II) Complexes of N-Heterocyclic Carbenes: Synthesis and Structural Characterization of Tetra-, Penta-, and Hexacoordinate Nickel Complexes. *Organometallics* **2009**, *28*, 1336−1349. (f) Petit, L.; Adamo, C.; Russo, N. Absorption spectra of first-row transition metal complexes of bacteriochlorins: A theoretical analysis. *J. Phys. Chem. B* **2005**, *109*, 12214−12221. (g) Bernardi, F.; Bottoni, A.; Rossi, I. A DFT investigation of ethylene dimerization catalyzed by Ni(0) complexes. *J. Am. Chem. Soc.* **1998**, *120*, 7770−7775.

(17) (a) Fujisawa, K.; Noguchi, Y.; Miyashita, Y.; Okamoto, K.-i.; Lehnert, N. Mononuclear and Binuclear Copper (I) Complexes Ligated by Bis (3, 5-diisopropyl-1-pyrazolyl) methane: Insight into the Fundamental Coordination Chemistry of Three-Coordinate Copper (I) Complexes with a Neutral Coligand. *Inorg. Chem.* **2007**, *46*, 10607−10623. (b) Praneeth, V.; Neese, F.; Lehnert, N. Spin Density Distribution in Five-and Six-Coordinate Iron (II)− Porphyrin NO Complexes Evidenced by Magnetic Circular Dichroism Spectroscopy. *Inorg. Chem.* **2005**, *44*, 2570−2572.

(18) Reed, A. E.; Curtiss, L. A.; Weinhold, F. Intermolecular interactions from a natural bond orbital, donor-acceptor viewpoint. *Chem. Rev.* **1988**, *88*, 899−926.

(19) Gonzalez, C.; Schlegel, H. B. An improved algorithm for reaction path following. *J. Chem. Phys.* **1989**, *90*, 2154−2161.

(20) (a) Cossi, M.; Scalmani, G.; Rega, N.; Barone, V. New developments in the polarizable continuum model for quantum mechanical and classical calculations on molecules in solution. *J. Chem. Phys.* **2002**, *117*, 43−54. (b) Miertuš, S.; Scrocco, E.; Tomasi, J. Electrostatic interaction of a solute with a continuum. A direct utilizaion of AB initio molecular potentials for the prevision of solvent effects. *Chem. Phys.* **1981**, *55*, 117−129.

(21) Dapprich, S.; Frenking, G. Investigation of donor-acceptor interactions: A charge decomposition analysis using fragment molecular orbitals. *J. Phys. Chem.* **1995**, *99*, 9352−9362.

(22) Vyboishchikov, S. F.; Frenking, G. Structure and Bonding of Low-Valent (Fischer-Type) and High-Valent (Schrock-Type) Transition Metal Carbene Complexes. *Chem.—Eur. J.* **1998**, *4*, 1428−1438.

(23) (a) Gorelsky, S.; Lever, A. Electronic structure and spectra of ruthenium diimine complexes by density functional theory and INDO/S. Comparison of the two methods. *J. Organomet. Chem.* **2001**, *635*, 187−196. (b) Gorelsky, S. *AOMix: Program for Molecular Orbital Analysis*; York University: Toronto, Canada, 1997.

(24) Gorelsky, S. I.; Ghosh, S.; Solomon, E. I. Mechanism of N_2O reduction by the μ_4-S tetranuclear CuZ cluster of nitrous oxide reductase. *J. Am. Chem. Soc.* **2006**, *128*, 278−290.